Archives of Hydro-Engineering and Environmental Mechanics
Vol. 57 (2010), No. 3-4, pp. 199–218

Application of Thermoporometry Based on Convolutive DSC to Investigation of Mesoporosity in Cohesive Soils

Tomasz Kozłowski, Izabela Babiarz, Edyta Grobelska

Department of Geotechnical and Water Engineering, Kielce University of Technology,
ul. Tysiąclecia Państwa Polskiego 7, 25-314 Kielce, Poland,
e-mails: tomkoz@tu.kielce.pl, IzabelaBabiarz@interia.pl, edytagrobelska@gmail.com

(Received March 10, 2010; revised June 24, 2010)

Abstract

In the method of thermoporometry, the characterization of pore space is done by analysis of thermal effects associated with freezing and melting of a liquid in the pores of the material under investigation. Thermoporometry seems particularly well suited to studies of wet porous samples in cases where the process of drying itself is able to destroy the original microstructure, as is the cohesive soils containing montmorillonite. In the paper, a variant of thermoporometry is given in which the blurred calorimetric peak is processed by use of a stochastic-convolutive analysis. As a result, a "sharp" thermogram of real thermal effects is obtained which can be easily transformed into a pore distribution curve. The preliminary results, obtained for samples of three monoionic montmorillonites at different water contents, indicate a greater resolution, sensitivity and precision than the classical thermoporometry using an unprocessed DSC signal. Phenomena corresponding to swelling have been detected in two individual regions on the differential pore distribution curves. The first is a dense spectrum for pores less than 15 nm. The second is a single peak for pores greater than 15 nm. Between the two regions the distribution decays to zero. Apparently, the point of the single peak maximum depends on the total water content, shifting rightward with increasing w. For the region below 20 nm, a strong effect of the kind of exchangeable cation can be observed. The results suggest swelling in the form with bivalent cations (Ca-montmorillonite) and contraction in the form with monovalent cations (Na- and K-montmorillonite).

Key words: pore distribution, thermoporometry, DSC (Differential Scanning Calorimetry), cohesive soils, montmorillonite

List of symbols

$a(T)$ – apparatus function,
C_f – heat capacity difference between water and ice per unit of ice crystal volume (Pa/K),
e – thickness of layer of the adsorbed water not undergoing phase changes (m),
$g(T)$ – calorimetric signal (J/K),

$h(T)$ – calorimetric signal corrected in relation to the base line (J/K),
K – cryoscopic Raoult coefficient,
L – latent heat of fusion of ice (J/kg),
m_0 – initial molality (mol/kg),
m_s – dry mass of soil sample (kg),
m_w – mass of water (kg),
$q(T)$ – temperature distribution of real thermal effects (J),
r_p – pore radius for an ice crystal in the cylindrical pore (m),
S – the total surface area of soil (m^2/kg),
S_f – entropy of fusion per unit of ice crystal volume (Pa/K),
T – temperature (°C), (K),
T_0 – water melting point at normal conditions (K),
T_{00} – solidification temperature of pure water in bulk at atmospheric pressure (K),
T_f, T_m – the freeezing and melting temperatures, respectively (K),
T_L, T_R – the initial and final temperatures of the DSC peak, recpectively (°C),
V_{ice} – volume of ice in pores (m^3),
V_p – pore volume (m^3),
V_{un} – volume of the unfreezable water (m^3),
w – total water content, % of dry soil mass,
w_{un} – unfreezable water content, % of dry soil mass,
γ – water/ice interface energy (N/m),
ρ_{ice} – density of ice (kg/m^3),
ρ_{un} – density of the unfreezable water (kg/m^3).

1. Introduction

The microstructure of porous media significantly affects the processes of adsorption and filtration. Knowledge of mechanisms governing filtration and adsorption in soil systems is essential in many problems of civil and environmental engineering (Romero et al 1999, Usyarov 2003). However, a macroscopic phenomenological approach is not sufficient in many cases. A proper modelling of mass and heat transport processes is not possible without an analysis on microstructural level. Detailed studies show that liquid transport characteristics of soils are predominantly affected by the pore size distribution (Velde et al 1996). Changes in pore space induced by the swelling-shrinkage process in a class of clays are a serious challenge in predictive modelling of hydraulic properties of such soils. Although the theory of crystal and osmotic swelling of clay minerals at the level of individual crystallite is relatively well developed, its application to prediction of hydraulic properties of expansive soils is still seriously limited (Tuller and Or 2003).

On the other hand, use of cohesive soils in industry and various civil and environmental engineering projects increases by the year. One of the reasons for this is the ease of their modification. Expansion/contraction, adsorption properties, colloid and rheological phenomena can be optimized according to intended use. Clays and cohesive soils are more and more frequently used as a blank for the production of hybrid organic-inorganic composites. The need to remove toxic compounds from the environment and to reduce the dispersion of pollutants in soil, water, and air is an additional driving force (Bergaya and Lagaly 2001). Bentonite, i.e. clay consisting mostly of montmorillonite, is used in the stablilization of drill holes and deep trenches for slurry walls. Recently, bentonites have been proposed as a barrier protection in nuclear waste storage (Montes et al 2003, Yang et al 2006). Clays are also used as environmental sealants, waste water treatment agents, oil and grease absorbents, binding agent in making molding sands, as filtration media in the production of edible oils and many others. In most of these cases, proper identification of microstructural and surface properties is particularly significant (Yang et al 2006).

Clays and cohesive soils are porous media; hence the identification of pore space is one of the most important elements in microstructure considerations. According to official documents of International Union of Pure and Applied Chemistry (Rouquerol et al 1994), in view of their sizes, pores are classified in different classes:

- Micropores have widths smaller than 2 nm.
- Mesopores have widths between 2 and 50 nm.
- Macropores have widths larger than 50 nm.

The following classification of techniques and methods for determination of morphological characteristics was constructed by combining the classifications given by Rouquerol et al (1994) and Leofanti et al (1998):

1. Nitrogen adsorption at 77 K (surface area, pore volume and size distribution)
   a) BET method (surface area)
   b) t-plot method (surface area, micropore and mesopore volume)
   c) as-plot method (surface area, micropore and mesopore volume)
   d) DR-plot (micropore volume)
   e) MP method (micropore volume and micropore size distribution)
   f) Horvath-Kavazoe method (micropore volume and micropore size distribution)
   g) DFT methods (pore volume and pore size distribution)
   h) BJH method (mesopore volume and mesopore size distribution)
   i) Gurvitsch volume method (micropore plus mesopore volume)
2. Krypton, argon and helium adsorption at low temperature (surface area and micropore volume)
3. Mercury porosimetry (meso and macropore volume and size distribution)
4. Incipient wetness method (total pore volume)
5. Picnometry (total pore volume)

6. Permeametry and counterdiffusion (average diffusive pore size and tortuosity factor)
7. Calorimetry
   a) Immersion calorimetry
   b) Gas adsorption calorimetry
   c) Liquid adsorption calorimetry
   d) Thermoporometry
8. Other methods
   a) Small angle X-ray and neutron scattering
   b) NMR and Xenon NMR
   c) Electron microscopy
   d) Molecular sieve method
   e) Gamma ray computed tomography (Pires et al 2005)

Almost all of the above-mentioned methods cannot be applied to wet porous systems. However, the pore system of clays is, in many cases, flexible and dependent on water content. In the method of thermoporometry proposed by Brun et al (1977), the characterization of pore space is done by way of freezing of a liquid in pores of the material under investigation. The change in the freezing temperature is related to pore size through the Gibbs-Thomson equation. Thermoporometry is a method to study mesoporosity. The porous solid saturated with a liquid is frozen to a temperature below the melting point of the liquid in bulk and then studied on heating by use of the Differential Scanning Calorimetry (DSC) technique. The depression of melting temperature ΔT is expressed by a function of the curvature, which enables to determine the pore size distribution (Kaneko 1994).

The advantage of this method is in providing the internal size of the pores (in the case of bottle-shaped pores) in the 1.5 to 150 nm range, whereas the techniques based on the N_2 desorption isotherm are able to provide the sizes of the pore-openings (Rouquerol et al 1994). Above all, however, thermoporometry seems particularly well suited for studies of wet porous samples in cases where the process of drying itself may destroy the original microstructure. In addition, thermoporometry makes it possible to determine the shape of pores by comparison of the data obtained on freezing with the data obtained on melting. In the beginning, thermoporometry was a relative method requiring calibration curves obtained from well recognized standard samples. The procedure presented by Brun et al (1977) made it an absolute method, enabling determination of pore distribution on the basis of theoretical relationships.

Recently, applications of thermoporometry to the investigation of pore spaces in various materials has been presented by many authors. In the works of Kaneko (1994) and Rouquerol et al (1994), limitations and merits of thermoporometry were analyzed alongside other methods such as molecular adsorption, x-ray diffraction and mercury porosimetry. Price and Bashir (1995) applied thermoporometry in determining of the location of the remainder of water in polyacrylonitryle (PAN). Titulaer et al (1995)

presented application of thermoporometry to investigation of silica hydrogels pores, obtaining information about the ice crystal radius, the ice pore volume, the pore shape and the ice-surface area. Beurroies et al (2004) proposed a methodology based on thermoporometry to evidence the hysteresis phenomenon observed between melting and solidification of a confined fluid.

Homshaw (1980) was the first to apply thermoporometry to soil-water systems. Basing on hysteresis between freezing and melting temperature in pores of two clays, he presented a theory of the effect of the shape of pores on temperatures of equilibrium freezing and melting. It has been stated that the analysis of low temperature endotherms yields a better assessment of the pore size distribution than the exothermic data (i.e. obtained on cooling). Homshaw and Cambier (1980) analyzed the pore size distribution curve obtained by use of N_2-adsorption, mercury porosimetry and DSC-based thermoporometry. The results confirmed that the water content of kaolin does not affect its porosity. On the basis of DSC data it was possible to obtain the pore size distribution curve from an individual sample.

In most publications regarding thermoporometry, the results are presented with same degree of reservation. As a rule, analysis is stopped at a qualitative or quasi-quantitative level. This is largely due to the occurrence of a broadening of the DSC peak, which will be discussed here further. In the paper, a proposal of a method is given, in which the broadened exothermal peak is processed by use of a stochastic-convolutive analysis. The result is a "sharp" thermogram of real thermal effects which can be easily transformed into the pore distribution curve.

2. Methodology

2.1. Convolutive Analysis of DSC Signal

The presented variant of thermoporometry is based on differential scanning calorimetry DSC. The term "scanning" relates to a continuous change in the temperature of the sample in an assumed range. The principle of the compensated scanning calorimeter is shown in Fig. 1. Two identical vessels, A with a sample and B without one, are located symmetrically inside calorimetric block K. Each vessel is equipped with an individual heat sensor and a micro-heater. The temperature of the block T_K can be changed at a constant rate (called the scanning rate v). Because of the thermal flow between the block and the vessels, their temperatures T_A and T_B change as well, where they would be equal in absence of the sample in vessel A.

The presence of the investigated sample leads to a temperature difference between the vessels. On warming, temperature T_A stays behind temperature T_B because of a difference in thermal capacities. In this case, the calorimeter control unit supplies the heater A with an additional power g. It can be proved that power g is proportional to the mass of sample m, its specific heat C and the scanning rate. The values of g, recorded by a microcomputer as a function of current sample temperature, are called the calorimetric signal $g(T)$. Because the specific heats of solids can be approximated

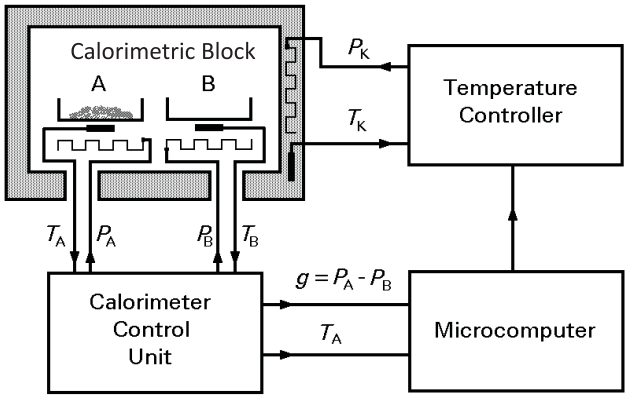

Fig. 1. Schematic diagram of the compensated scanning calorimeter

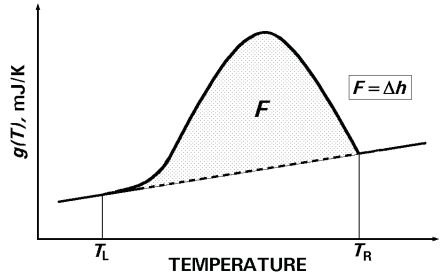

Fig. 2. Heat of phase change Δh as the area of peak on the calorimetric signal plot

by a simple linear function, the plot of $g(T)$ in the temperature interval before the beginning of the phase transitions represents a straight line called the reference or base line. A phase change taking place in the vessel A causes an increase of $g(T)$ in the case of the endothermic process of ice melting. It appears as a peak on the plot of the calorimetric signal. The field of the peak is equal to the total heat of phase transition Δh (or in other words – change of enthalpy of the system):

$$\Delta h = \int_{T_L}^{T_R} h(T)dT, \tag{1}$$

where $h(T)$ is the function $g(T)$ corrected in relation to the base line and T_L and T_R are respectively the initial and final temperatures of the peak (Fig. 2).

Independent of the apparatus construction, thermograms obtained during the DSC runs are not real thermal flux curves connected with the investigated process. Existence of thermal resistance between the sample and a heat sensor leads to an effect

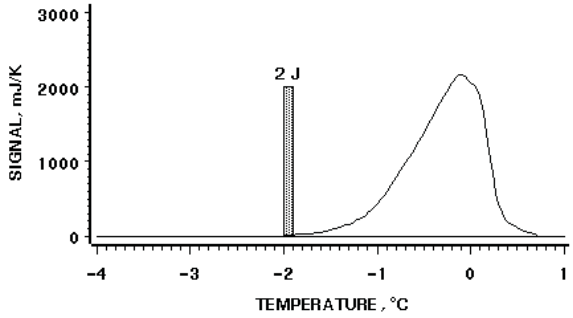

Fig. 3. Response of calorimeter to a single thermal impulse

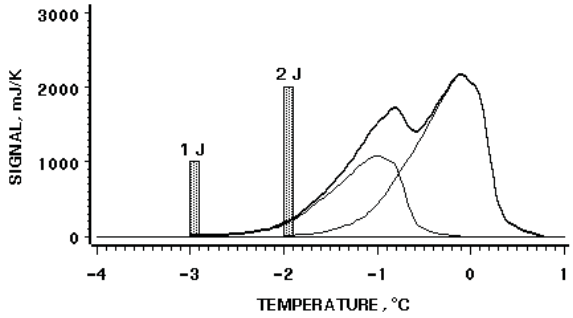

Fig. 4. Response of calorimeter to two thermal impulses as a superposition

called the broadening of the experimental curve (Hemminger and Höhne 1984). Let us analyze a thermal impulse connected with a phase transition of a crystalline substance. The impulse, in reality yielded at a strictly determined temperature T_0, called the melting or freezing point, is recorded as a peak, only the starting point of which is at T_0, and the width is an increasing function of the scanning rate (Fig. 3). More thermal impulses yield a peak as the superposition of a number of peaks (Fig. 4).

Normalisation of the function from Fig. 3 in relation to the total thermal effect Δh and the temperature T_0 gives an apparatus function $a(T)$ connected with the construction of a given calorimeter and which is capable of being estimated experimentally (Kozlowski 2003):

$$a(T_0 - T) = \frac{h(T_0 - T)}{\Delta h}, \tag{2}$$

where $h(T)$ is the observed heat flux thermogram, in J/K, and Δh is the total thermal effect absorbed or yielded at the temperature T_0, in J.

The apparatus function given by Eq. (2) can be easily determined experimentally, by melting a small portion of ice. In the present experiment, the apparatus function

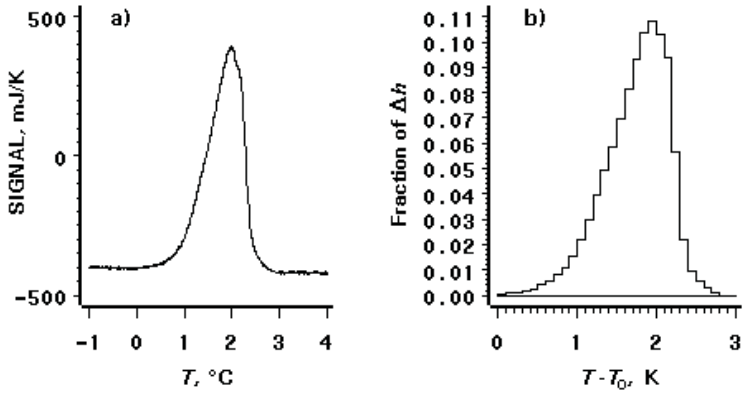

Fig. 5. The apparatus function: a) the initial corrected peak $h(T)$ recorded for a sample of pure ice; b) the apparatus function $a(T)$ determined exact to one tenth of a Kelvin

$a(T)$ was determined on a base of thermograms obtained by melting six samples of pure ice with the scanning rate equal to 0.5 K/min. For the masses between 0.5 mg and 4.0 mg the observed shapes of the peak were very similar. Error in determination of the melting point comprehended as the peak starting point was less than 0.1 K in all instances and error in determination of the latent heat was less than 1%. One of the peaks, obtained for a sample of 2.20 mg, was chosen for creation of the apparatus function. The main reason for such a choice was the excellent results obtained for this sample: the melting point $T_0 = +0.05°C$ and the latent heat of fusion $L = 333.32$ J/g. The observed peak was divided into fields 0.1 K in width. The number of the fields, which corresponds with the value of l in Eq. (4), equalled 28. The area of each field was divided by the total field of the peak. Thus, the obtained apparatus function represents the distribution of fractions of the total heat of fusion of ice at 0°C, which are observed at the wide temperature interval above as an endothermic peak (Fig. 5).

In terms of mathematics, the observed function $h(T)$ is a convolution of the function of the real thermal effects $q(T)$ and the apparatus function $a(T)$:

$$h(T) = \int_{-\infty}^{\infty} a(T - T')q(T')dT'. \tag{3}$$

Then, the problem of finding the function of the real heat flux consists in solving Eq. (3) in relation to $q(T)$ when the functions $h(T)$ and $a(T)$ are known. It is possible to solve the problem by use of Fourier transforms, but the method is not always convergent, especially when working on experimental data with random noise. Thus we decided to work out a method based on a numerical analysis of the square deviations of the observed function $a(T)$ and convolution of the apparatus function $a(T)$ with functions $q_i(T)$, being successive approximations of the real function $q(T)$.

The observed function of heat flux $h(T)$ (or the calorimetric peak) was divided into a number of finite elements of width $\Delta T_i = T_{i+1} - T_i$, each with a constant value of thermal flux $h(T_i)$. This applied to the apparatus function $a(T)$ as well. Eq. (3) in a finite differences form can be written as follows (Kozlowski 2003):

$$h(T_j) = \sum_{i=1}^{n} \sum_{j=i}^{i+m-1} a(T_j - T_i) q(T_i) \Delta T_i, \tag{4}$$

where n is the number of elements of the observed function and l is the number of elements into which the apparatus function was divided.

A good approximation of the function $q(T_i)$ was determined by producing its possible forms $q_k(T_i)$, making their convolutions $h_k(T_i)$ with the apparatus function $a(T_i)$ according to Eq. (5), and analyzing the following sums of square deviations:

$$D_k = \sum_{i=1}^{n} (h(T_i) - h_k(T_i))^2. \tag{5}$$

The value of D_k reaches a minimum for the best approximation of $q(T_i)$. The values of the obtained real function of heat $q(T_i)$ multiplied by the widths of temperature intervals ΔT_i express a distribution of the conventional heat impulses attributed to the temperature intervals. The temperature of the last non-zero impulse is the temperature of the end of melting T_0 or the melting point, with an accuracy equal to the length of the temperature interval ΔT_i.

During calculations, the obtained corrected peak $h(T)$ is divided into n fields 0.1 K in width. A computer program calculates the total heat Δh of phase changes as the field of the peak. Next, a form of the function $q_k(T_i)$ is created by an attribution of fractions of the total heat to temperatures T_i and division of the fractions by $\Delta T_i = 0.1$ K. At successive stages of computations, elementary "bricks" of the fractions decrease from 20% of Δh to 0.625% of Δh. According to Eq. (4), the convolution of $q_k(T_i)$ with $a(T_i)$ is made, and fitting is checked by use of Eq. (5). A pass to another stage occurs after finding such a distribution of the fractions which gives a minimum of D_k. The transformation of the originally observed peak $h(T)$ into the thermogram of real thermal effects $q(T)$ is shown in Fig. 6.

2.2. Obtaining Pore Size Distribution from the Thermogram of Real Thermal Effects

The thermogram of real thermal effects $q(T)$ can consequently be used to analyse of the pore space according to the following procedure.

For the soil-water system, the main thermoporometry equation can be written as follows (Fabbri et al 2006):

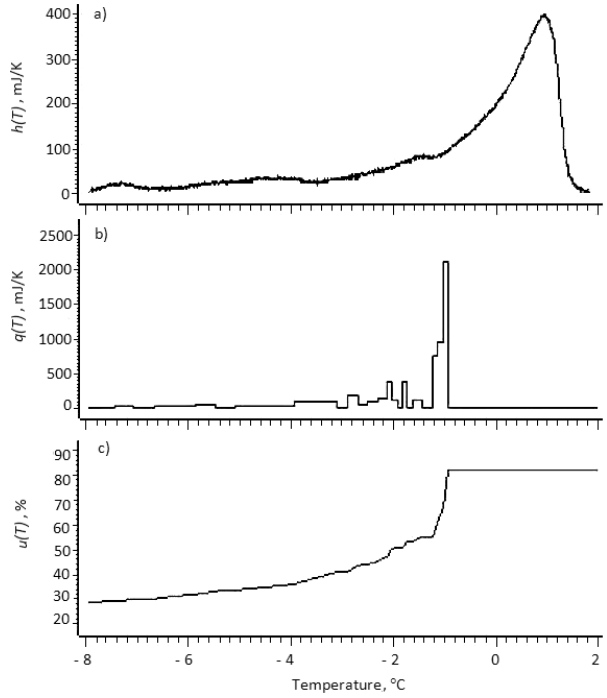

Fig. 6. An example of transformation of the observed peak into the unfrozen water content curve: a) initial peak $h(T)$ corrected in relation to the fluent base line; b) the thermogram of real thermal effects $q(T)$; c) the unfrozen water content curve

$$T_f = g^{-1}\left(\frac{2\gamma}{r_p - e}\right), \tag{6}$$

$$T_m = g^{-1}\left(\frac{\gamma}{r_p - e}\right), \tag{7}$$

where T_f and T_m are the freeezing and melting temperatures, respectively; r_p is the corresponding pore radius for an ice crystal in the cylindrical pore, being in equilibrium with liquid water in adjacent pores; γ is the water/ice interface energy; e is the thickness of layer of the adsorbed water not undergoing phase changes and g^{-1} is a function inverse to a state function given by Fabbri et al (2006) in the following form:

$$g(T) = S_f(T_0 - T) + C_f\left(T - T_0 + T\ln\left(\frac{T_0}{T}\right)\right), \tag{8}$$

where S_f is the entropy of fusion per unit of ice crystal volume, C_f is the heat capacity difference between water and ice per unit of ice crystal volume and T is the water freezing point at normal conditions.

It can be assumed that $S_f \approx 1.2$ MPa/K and $C_f \approx 2.1$ MPa/K (Brun et al 1977) and the temperature T_0 is expressed by Raoult law as

$$T_0 = T_{00} - K \cdot m_0, \tag{9}$$

where T_{00} is the solidification temperature of pure water in bulk at atmospheric pressure (= 273.15 K), m_0 is the initial molality (about 1 mol/kg for cement paste older than 90 days; Fabbri et al 2006) and K is the cryoscopic Raoult coefficient, dependent on the solvent and irrespective to solute. In the case of water solvent, $K = 1.86$ (Zuber and Marchand 2000).

For the water/ice interface energy in Eqs. (6) and (7), Fabbri et al (2006) proposed the following simplified equation:

$$\gamma = 36 + 0.25 \cdot (T - T_{00}), \tag{10}$$

in which γ is expressed in N/m.

In order to determine the value of e, the following procedure was applied. Firstly, the content of the unfreezable water w_{un} was computed as the difference between the total water content and the ice content, which can be expressed as (Kozlowski 2003)

$$w_{un} = w - \frac{100 \cdot \Delta h}{L \cdot m_s}, \tag{11}$$

where w is the water content (%), Δh is the total heat of phase transition obtained accordingly to Eq. (1) (J); L is the latent heat of fusion of ice (J/kg) and m_s is the dry mass of soil sample (kg).

Now the volume of the unfreezable water can be determined as

$$V_{un} = \frac{w_{un} m_s}{100 \rho_{un}} = S \cdot m_s \cdot e, \tag{12}$$

which allows to determine the layer thickness of the adsorbed water:

$$e = \frac{w_{un}}{100 \rho_{un} S}, \tag{13}$$

where ρ_{un} is density of the unfreezable water and S is the total surface area of soil.

Hence, Eqs. (6)–(13) make it possible to relate the temperatures of phase changes to the pore radius. Subsequently, the value of thermal effect associated with a given temperature can be used to calculate the quantity of water undergoing phase changes:

$$m_w(\Delta T_i) = \frac{q(\Delta T_i)}{L(T_i)}, \tag{14}$$

where $m_w(\Delta T_i)$ is the amount of water undergoing phase change when temperature changes by ΔT_i; $q(\Delta T_i)$ is the thermal effect associated with the temperature change ΔT_i (according to Eq. (4)) and $L(\Delta T_i)$ is an average value of latent heat of fusion in

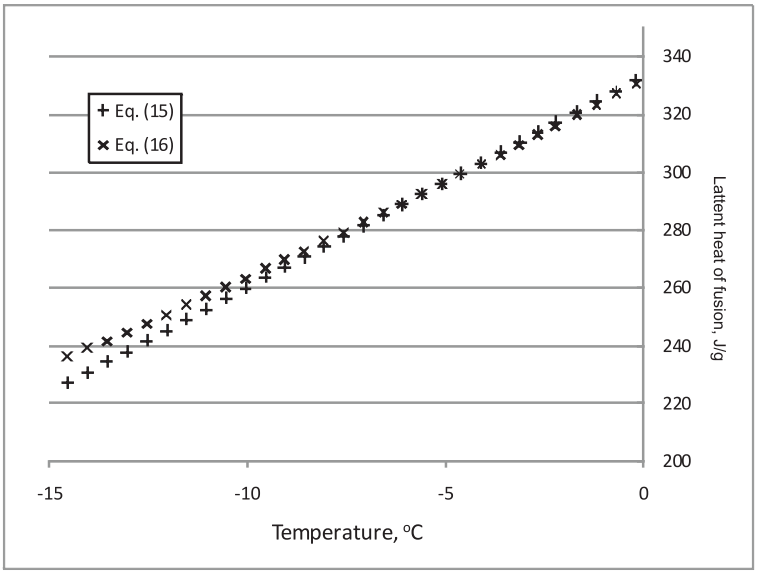

Fig. 7. Temperature dependence of latent heat of fusion of ice according to Eqs. (15) and (16)

the temperature range ΔT_i. In the presented calculations, the length of the temperature interval ΔT_i was equal to 0.1 K, which was explained in Section 2.1.

It is known that the value of the latent heat of fusion of ice L decreases with decreasing temperature. Horiguchi (1985) presented the following formula, obtained experimentally for water freezing on silica gels:

$$L(T) = 7.3 \cdot T + 334, \tag{15}$$

where $L(T)$ is the latent heat of fusion of ice at temperature T in J/g and T is temperature in °C.

Similar values are given by the following quadratic equation (Price and Bashir 1995):

$$L(T) = 0.0556T^2 + 7.42T + 332, \tag{16}$$

which is shown in Fig. 7. The differences observed in Fig. 7 for temperatures below −10°C seem insignificant, because the intensity of the phase changes decreases with temperature. Decreasing $q(\Delta T_i)$ in Eq. (14) with temperature results in a corresponding diminished influence of varying values of $L(T_i)$ at lower temperatures. The computations reported below were made by use of Eq. 16.

Now, Eq. (14) can be used to determine the change of pore ice volume on melting when temperature rises by ΔT_i:

$$V_{ice}(\Delta T_i) = \frac{q(\Delta T_i)}{L(T_i) \cdot \rho_{ice}}, \tag{17}$$

which, via Eqs. (7), (8) and (13), can be attributed to the volume of pores of a given radius r_p.

Finally, the normalized pore size distribution curve is calculated as follows:

$$\frac{dV_p}{dr_p} \cong \frac{V_{ice}(\Delta T_i)}{m_s \cdot r_p(\Delta T_i)}, \tag{18}$$

where $r_p(\Delta T_i)$ is the change of pore radius associated with the change of temperature by ΔT_i.

3. Results and Analysis

3.1. Materials and Experimental Procedure

For this study, homoionic forms of montmorillonite were used. The forms were obtained from natural bentonite from Chmielnik in Poland by repeated saturation of the fraction less then 0.063 mm and subsequent purifying from solutes by diffusion. The soil pastes were then dried at room temperature to the required total water content and stored in closed vessels for about three weeks before the experiment. The total water contents varied between approximately $w = 0.5w_P$ and $w = 1.5w_L$. The properties of the soils are given in Table 1.

Table 1. Soil properties

Type of soil	C.E.C [meq/100g]	Fraction $< 2\mu$ m [%]	Consistency limits		Spec. surface [m^2/g]	
			w_P [%]	w_L [%]	External	Total
Ca-montmorillonite	108.05	34	69.7	106.8	122	732
Na-montmorillonite	111.12	92	86.5	253.7	110	644
K-montmorillonite	49.98	30	66.0	93.2	56	336

Aluminium sample pans were weighed and filled with the soil pastes, sealed hermetically and weighed again. The masses of the soil samples were determined by differentiation and amounted to approximately 10 mg. A thin layer of the soil paste covered only the bottom of the pan which ensured a very good exchange of heat. A quasi-uniform thermal field within the sample is the necessary condition of the presented method. The Unipan-Thermal differential scanning calorimetry system Model 607 with an LN_2 cooling system was used in the experiments. The samples were cooled with the scanning rate 1 K/min to −28°C and then warmed with the scanning rate 0.5 K/min to +10°C at a calorimeter sensitivity of 5 mW. After the experiment, pinholes were punched in the sample covers and the total water content was determined by drying to a constant mass at 110°C.

Only results obtained during the warming DSC run were analyzed, ipso facto the non-equilibrium phenomena connected with supercooling have been excluded.

3.2. Exemplary Results

In the light of preliminary results, the presented method of pore network investigation seems fully reliable. Firstly, the obtained curves of pore distribution are surprisingly sharp, which is impossible to obtain by any other method. Secondly, the results are repeatable, which is apparent from comparison of the differential pore distribution curves obtained for samples of the same clay with similar water contents (Fig. 8).

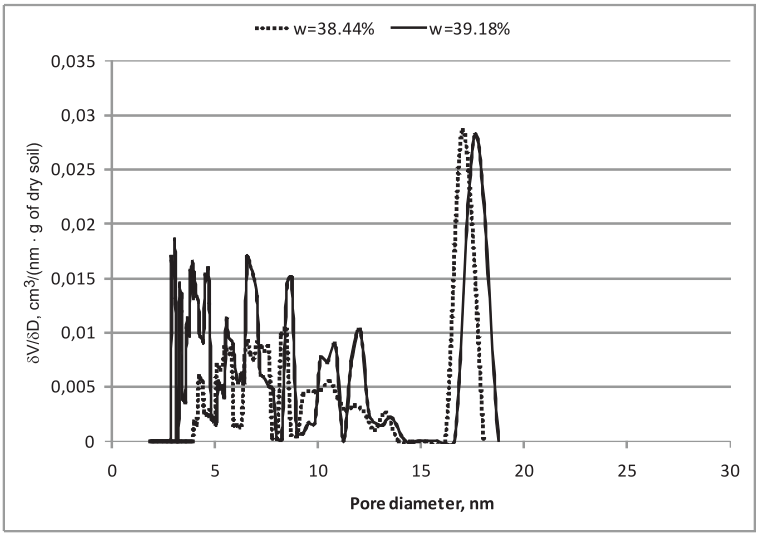

Fig. 8. Comparison of two differential pore distribution curves obtained at two similar water contents for Ca-montmorillonite

Two main regions can be distinguished on the differential pore distribution graphs (Figs. 9–11). The first is the dense spectrum for pores less than 15 nm. The second is a single peak for pores greater than 15 nm. Between the two regions, the distribution decays to zero. Apparently, the point of the single peak maximum depends on the total water content, shifting rightward with increasing w. The sensitivity of the method proved sufficient to detect the very small shift corresponding to the increase of the water content from 38.44% to 39.18% (Fig. 8). In contrast, the points of peak maxima in the region of pores less than 20 nm seem independent of such a small water content increment, however; the peak values increase with increasing water content. The effect of the water content can be observed for a wide range in Figs. 9–11, where the differential pore volume distribution curves obtained for three homoionic montmorillonites are shown. The corresponding cumulative pore volume distribution data are shown in Figs. 12–14. The shift of maxima in the range of larger mesopores (> 20 nm) and an insignificant effect on the pore distribution in the range < 20 nm is still observed. In the case of each soil, the characteristic 'wandering' peak can be distinguished, the maximum point of which is strictly related to the water content

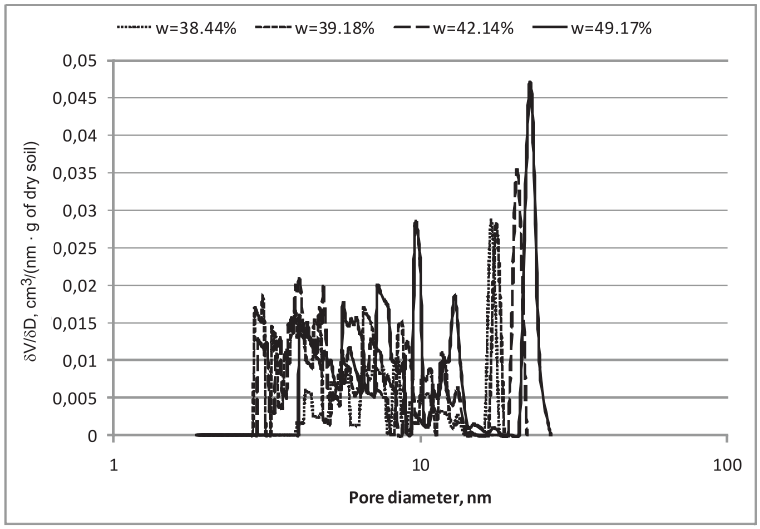

Fig. 9. Differential pore distribution curves obtained at four water contents for Ca-montmorillonite

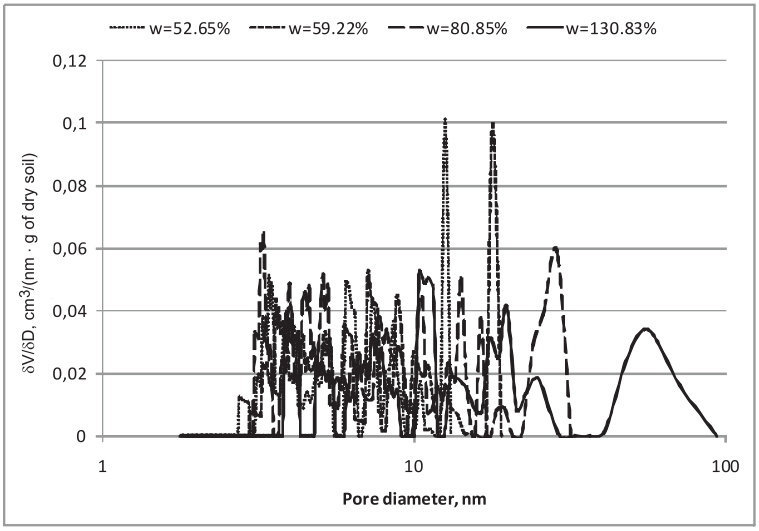

Fig. 10. Differential pore distribution curves obtained at four water contents for Na-montmorillonite

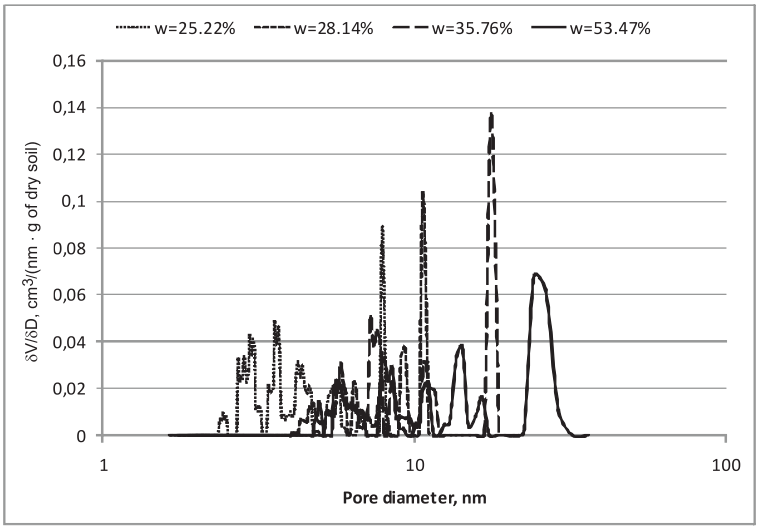

Fig. 11. Differential pore distribution curves obtained at four water contents for K-montmorillonite

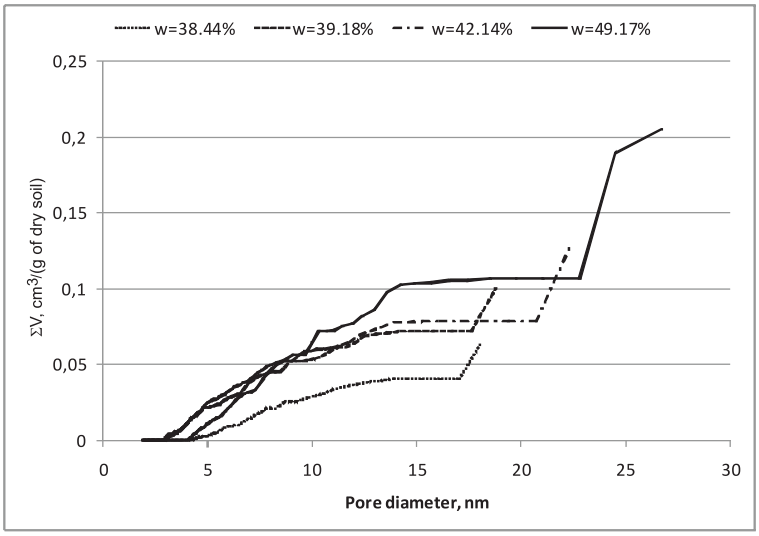

Fig. 12. Cumulative pore distribution curves obtained at four water contents for Ca-montmorillonite

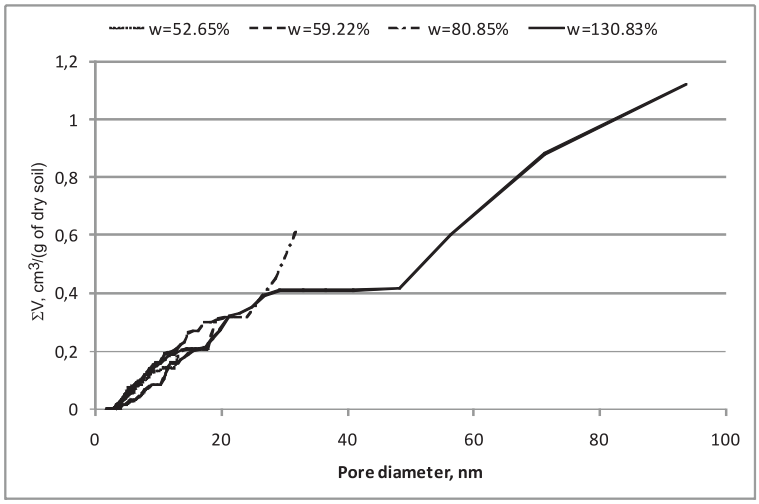

Fig. 13. Cumulative pore distribution curves obtained at four water contents for Na-montmorillonite

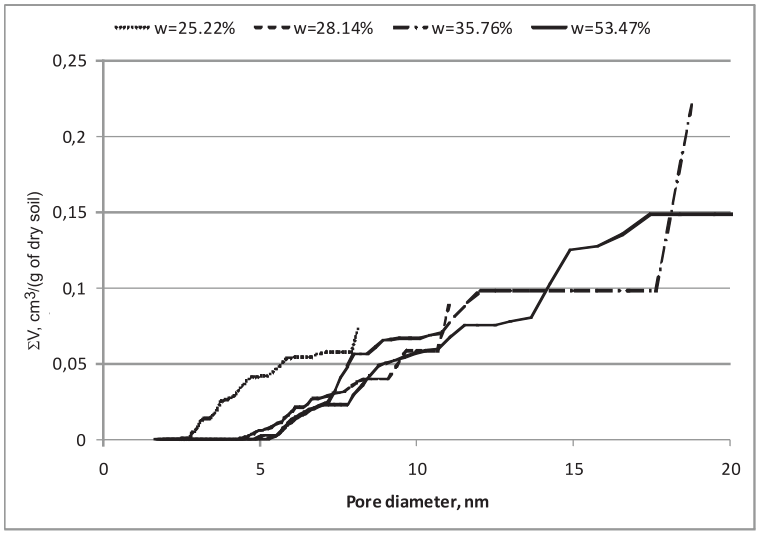

Fig. 14. Cumulative pore distribution curves obtained at four water contents for K-montmorillonite

and increases with increasing water content. However, it seems that the peak value, corresponding to the pore volume increment, only behaves in this manner at water contents lower than a boundary water content. It can be observed in Figs. 10 and 11 for Na- and K-montmorillonites. In both the monovalent forms of montmorillonite, the maxima of the 'wandering peak' begin to decrease in samples with water content higher than approximately 0.8 w_P. Such a value was exceeded in K-montmorillonite in the case of the sample with w = 53.49% (= 0.81 w_P) and in Na-montmorillonite in samples with w = 80.85% and w = 130.8% (0.93 and 1.51 respectively). Notice that all the water contents in Ca-montmorillonite samples in Fig. 10 do not exceed the value 0.8 w_P. In Ca-montmorillonite samples with high water contents, not shown in the figure, the effect of broadening and lowering of the 'wandering peak' was observed as well. Apparently, the pore volume increment at higher water contents includes a wider spectrum of pore sizes. This conclusion can be supported by comparison with the cumulative curves in Figs. 13 and 14. Probably the phenomenon in question is independent of the nature of the exchangeable cation and, in some way, is related to swelling.

For the region less than 20 nm, a strong effect of the kind of exchangeable cation is apparent. In K-montmorillonite, a characteristic phenomenon of shifting leftward in the case of the smallest water content is observed (Fig. 11). Paradoxically, the total pore volume in the range < 7 nm is greater at the lowest water content than at higher water contents (Fig. 14), which is in contrast to the other forms. Assuming that the observed evolution of the microstructure with respect to changing water content is due to swelling phenomena, such a behaviour of potassium montmorillonite could involve contraction in the region of the smallest mesopores. Contrariwise, an expansion is observed in this small mesopore range for the calcium form of montmorillonite (Fig. 12). Finally, the cumulative curves obtained for sodium montmorillonite suggest a lack of swelling phenomena in the region of mesopores at water contents less than the plastic limit (Fig. 13). However, the cumulative pore distribution curve attained at w = 130.83% suggests contraction in the smallest mesopores region and a significant swelling in the region of mesopores > 50 nm, which brings Na-montmorillonite closer to K-montmorillonite, the other monovalent cation form of montmorillonite tested.

4. Conclusions

1. The application of the stochastic convolution method to analysis of DSC (Differential Scanning Calorimetry) signal enables determination of the real heat flux function $q(T)$ absorbed by the frozen soil sample during the warming DSC run. It is based on searching for a distribution of "heat impulses" in relation to temperature, which, convoluted with the apparatus function $a(T)$, gives a minimal deviation from the observed heat flux function $h(T)$.

2. The presented version of thermoporometry based on the real heat flux function $q(T)$ is characterized by greater resolution, sensitivity and precision than the classical thermoporometry using the unprocessed DSC signal.
3. The method seems particularly useful in order to study the effect of the water content on the swelling clay microstructure. The preliminary results, obtained for samples of three monoionic montmorillonites at different water contents, indicate the presence of two individual regions on the differential pore distribution curves. The first is the dense spectrum for pores less than 15 nm. The second is a single peak for pores greater than 15 nm. Between the two regions the distribution decays to zero. Apparently, the point of the single peak maximum depends on the total water content, shifting rightward with increasing w. For the region less than 20 nm, a strong effect of the kind of exchangeable cation can be observed. The results suggest swelling in the form with bivalent cations (Ca-montmorillonite) and contraction in the form with monovalent cations (Na- and K-montmorillonite).

Acknowledgments

This work was partially supported by the Polish Ministry of Science under grant N N525 349538 and the Operational Programme Human Capital (OP HC), contract number UDA-POKL.04.01.01-00-175/08-00.

Co-author of the article, Edith Grobelska, receives a scholarship financed by the European Union under the European Social Fund project "Didactic Potential Development Program at the Kielce University of Technology – education, where success". The Operational Programme Human Capital, contract number UDA-POKL.04.01.01-00-175/08-00.

References

Bergaya F., Lagaly G. (2001) Surface modification of clay minerals, *Applied Clay Science*, **19**, 1–30.

Beurroies I., Denoyel R., Llewellyn P., Rouquerol J. (2004) A comparison between melting-solidification and capillary condensation hysteresis in mesoporous materials: Application to the interpretation of thermoporometry data, *Thermochimica Acta*, **421**, 11–18.

Brun M., Lallemand A., Quinson J.-F., Eyraud Ch. (1977) A new method for the simulta-neous determination of the size and the shape of pores: the thermoporometry, *Thermochimica Acta*, **21**, 59-88.

Fabbri A., Fen-Chong T., Coussy O. (2006) Dielectric capacity, liquid water content, and pore structure of thawing–freezing materials, *Cold Regions Science and Technology*, **44**, 52–66.

Hemminger W., Höhne G. (1984) *Calorimetry: Fundamentals and Practice,* Verlag Chemie GmbH.

Homshaw L. G. (1980) Freezing and melting temperature hysteresis of water in porous materials: Application to the study of pore form, *European Journal of Soil Science*, **31**, 399–414.

Homshaw L. G., Cambier P. (1980) Wet and dry pore size distribution in a kaolinitic soil before and after removal of iron and quartz, *European Journal of Soil Science*, **31**, 415–428.

Horiguchi K. (1985) Determination of unfrozen water content by DSC, *Proc.* 4^{th} *Int. Symp. Ground Freezing*, Sapporo, A. Balkema, Rotterdam, **1**, 33–38.

Kaneko K. (1994) Determination of pore size and pore size distribution, Part 1: Adsorbents and catalysts, *Journal of Membrane Science*, **96**, 59–89.

Kozlowski T. (2003) A comprehensive method of determining the soil unfrozen water curves, Part 1: Application of the term of convolution, *Cold Regions Science and Technology*, **36**, 71–79.

Leofanti G., Padovan M., Tozzola G., Venturelli B. (1998) Surface area and pore texture of catalysts, *Catalysis Today*, **41**, 207–219.

Montes G., Duplay J., Martinez L., Mendoza C. (2003) Swelling–shrinkage kinetics of MX80 bentonite, *Applied Clay Science*, **22**, 279–293.

Pires L. F., Bacchi O. O. S., Reichardt K. (2005) Gamma ray computed tomography to evaluate wetting/drying soil structure changes, *Nuclear Instruments and Methods in Physics Research, B* 229, 443–456.

Price D. M., Bashir Z. (1995) A study of the porosity of water plasticised polyacrylonitrile films by thermal analysis and microscopy, *Thermochimica Acta*, **249**, 351–366.

Romero E., Gens A., Lloret A. (1999), Water permeability, water retention and microstructure of unsaturated compacted Boom clay, *Engineering Geology*, **54**, 117–127.

Rouquerol J., Avnir D., Fairbridge C. W., Everett D. H., Haynes J. H., Pernicone N., Ramsay J. D. F., Sing K. S. W., Unger K. K. (1994) Recommendations for the characterization of porous solids (Technical Report), *Pure & Applied Chemistry*, **66** (8), 1739–1758.

Titulaer M. K., van Miltenburg J. C., Jansen J. B. H., Geus J. W. (1995), Thermoporometry applied to hydrothermally aged sillica hydrogels, *Recl. Trav. Chim. Pays-Bas*, **114**, 361–370.

Tuller M., Or D. (2003) Hydraulic functions for swelling soils: Pore scale considerations, *Journal of Hydrology*, **272**, 50–71.

Usyarov O. G. (2003), Experimental study of small-scale spatial variation in filtration coefficient using tracer method, *Colloid Journal*, **65**, 100–104.

Velde B., Moreau E., Terribile F. (1996) Pore networks in an Italian vertisole: Quantitative characterization by two dimensional image analysis, *Geoderma*, **72**, 271–285.

Yang Tao, Xiao-Dong Wen, Junfen Li, Liming Yang (2006) Theoretical and experimental investigations on the structures of purified clay and acid-activated clay, *Applied Surface Science*, **252**, 6154–6161.

Zuber B., Marchand J. (2000) Modeling the deterioration of hydrated cement systems exposed to frostaction, Part 1: Description of the mathematical model, *Cement and Concrete Research*, **30**, 1929–1939.